Measurement of three-dimensional volumetric displacement fields in structural porous adhesive joints, under tensile and tensile-shear load, by means of in-situ X-ray microtomography

C. Badulescu, V. Dumont, M. Diakhaté, M. Bunea, G. Stamoulis, J. Adrien, E. Maire, D. Thévenet

Measurement of three-dimensional volumetric displacement fields in structural porous adhesive joints, under tensile and tensile-shear load, by means of *in-situ* X-ray microtomography

C. Badulescu[1*], V. Dumont[2], M. Diakhaté[3], M. Bunea[4,5], G. Stamoulis[3], J. Adrien[6], E. Maire[6] and D. Thévenet[1]

[1]ENSTA Bretagne, UMR CNRS 6027, IRDL, F-29200 Brest, France
[2]Safran Reosc - Engineering & Integration Department - 91280 St Pierre-du-Perray, France
[3]Univ. Bretagne Occidentale, UMR CNRS 6027, IRDL, F-29200 Brest, France
[4]"Dunarea de Jos", University of Galati, Cross–Border Faculty, Department of Applied Sciences, Galati, Romania
[5]Cahul State University "B. P. Hasdeu", Faculty of Economics, Engineering and Applied Sciences, Department of Engineering and Applied Sciences, Cahul, Republic of Moldova
[6]Univ. Lyon, INSA Lyon, UMR CNRS 5510, Laboratoire MATEIS, F-69621, Villeurbanne Cedex, France

Keywords: Structural bonding, Volumetric displacement fields, X-ray microtomography, Pores, Image processing

[*] **Corresponding author:** *claudiu.badulescu@ensta-bretagne.fr*

Abstract

Nowadays, structural bonding is increasingly used for its advantages over conventional joining methods such as riveting or welding. Bonding defects (incomplete polymerization, gradient of mechanical properties, and presence of pores, *among others.*) can significantly impact the mechanical behavior of these assemblies. Among these defects, the presence of pores, detectable by means of X-ray microtomography measurements, could have a significant influence on the mechanical strength of a bonded structure (reduction of the useful section, questioning of the continuity of the joint, and stress concentration, among others). The study of these pores populations by means of microtomographic measurements, as well as their evolution under mechanical stress, can therefore provide valuable information regarding the mechanical behavior. These data can provide information on (i) the mechanical behavior on a microscopic scale, (ii) the identification of mechanisms of damage and failure of the adhesive joint, or (iii) the measurement of volume displacement fields. In this work, a method for calculating volume displacement fields in an adhesive joint is presented, using the detected pores as markers. The robustness, limits, and effects of different parameters (noise, voxelization, among others.) on this algorithm are identified on synthetic data

representative of an adhesive joint. Finally, the validation of the method is based on interrupted tests on relatively small bonded specimens (called mini-Scarf) under tensile and tensile-shear loads.

1 Introduction

Structural bonding is becoming more and more essential in many sectors (aeronautics, automotive, energy, *among others*.) when it comes to assembling various mechanical parts. Indeed, this technique has many advantages, such as i) a significant reduction in the mass of the structures compared to traditional assembling methods (welding, bolting, *among others*.), ii) the possibility of easily assembling different materials or materials unsuitable for welding, and iii) interesting stress redistribution among the structure under mechanical loading. Consequently, this technique has been the subject of numerous studies and works, both from the point of view of experimental characterization and mechanical behavior modeling [1, 2, 3, 4].

To obtain the measurements necessary for these mechanical characterizations, many techniques, more or less expensive and advanced, are available. These techniques, ranging from the use of a simple extensometer to the development of digital image correlation algorithms, make it possible to obtain information (punctual or fields), on the surface of the analyzed sample. In many cases, and *a fortiori* in the field of structural bonding where mainly assemblies are characterized, the deformations occurring at the surface can be quite different from those occurring at the core [5, 6, 7]. A popular way of obtaining data at the core of a material is to use X-ray tomography measurements [8, 9, 10, 11].

Derived from the medical field [12], X-ray tomography has been extensively used in materials science for the past decades, for the many advantages it features. This technique is nondestructive, which is obviously of great interest for *in-situ* testing [9]. Moreover, the provided data are three-dimensional and often come with a fairly interesting voxel size (possibly less than 1 µm, depending on the tomograph and the region of interest of the studied object). Extensively used on metals at first, for pores

[13] and damage detection [14], this technique has been applied to a variety of materials to this day. Some of these works exploit the non-destructive aspect of X-ray tomography to perform *in-situ* material characterization on metals [15] and metal matrix composites [8] loaded in tension, or on compressed syntactic foams [16].

These structures are prone to feature voids and other defects in their bulk, which are easily detected using X-ray micro-tomography. On this matter, Pavan *et al.* [17] characterized the porous structure of laser-sintered polyamide structures, for different characteristic sizes. It was found that the size of the structure had a significant influence on the characteristics of the voids created during the process. More recently, Wang *et al.* [18] proposed a micromechanical model to characterize the mechanical behavior of 3D-printed polymers, supported by X-ray microtomography measurements. It was found that the specimens featuring the lowest porosity had the best mechanical properties. It should however be noted that the finite element computations carried out in this study were performed under 2D assumptions, with little regard for the shape and the spatial distribution of the pores. Specifically, on adhesives and bonded assemblies, the published papers are relatively scarce. However, a few studies released in the past years can be found, that take advantage of microtomography to characterize the porous nature of adhesive joints. For instance, Dumont *et al.* [19] studied the effect of the curing temperature on the characteristics of the pore populations detected in adhesive joints. The authors also studied the influence of mechanical stress on the pores in adhesive joints during *in-situ* tensile tests coupled with X-ray microtomography, for various configurations [20, 21]. It was found that the pores are subject to changes under loading, which depend on the characteristics of the considered populations. The coalescence phenomena were observed above a certain stress threshold. Other studies can be found, even though they are not focused on the characterization of the pore populations encountered in adhesive joints. For example, Schwarzkopf [22] described wood-adhesive interfaces from a micromechanical standpoint, using microtomography measurements. McKinley *et al.* [23] used X-ray tomography to analyze the bonding process and the penetration of the adhesive in the fibrous structure of wooden parts. The authors however encountered experimental difficulties related to the materials

investigated, including a lack of accuracy and sometimes poor greyscale levels. The study of the porosity of bonded joints in assemblies is still fairly new, and even more so under loading.] Nevertheless, studying the evolution of pores present in the adhesive under the effect of mechanical loading will enable us to understand the evolution of the microstructure, with the aim of subsequently improving the mechanical strength of bonded structures. This improvement can intervene on two levels: (i) X-ray tomography provides measurements at a scale usually disregarded for the study of bonded assemblies (*i.e.* microscopic scale), and (ii) it also provides data from the bulk of the joints, while traditional techniques (extensometer, Digital Image Correlation, *among others*.) focus on surface measurements. Consequently, tracking pore-related quantities during mechanical tests is quite an interesting approach to gathering data from the joints in their entirety.

In the following study, the pores detected in adhesive joints by means of X-ray microtomography were individually tracked, in order to compute their displacements during tensile mechanical experiments. By doing so, it was then possible to estimate the volumic displacement field occurring in the adhesive, which can be useful for instance to detect crack initiation or debonding (leading to large localized displacements) or to enrich experimental databases used to identify the parameters of mechanical behavior laws. It should be noted that only the feasibility of the method is addressed in this work. This study is divided into five parts, addressing respectively, the experimental methodology, the processing technique applied to the tomographic data, the validation of the suggested approach on representative artificial datasets, and the experimentally measured displacement fields.

2 Experimental procedure

2.1 Preparation of the samples

Mini-scarf samples were used, and two configurations were considered for this study. The first one, referenced mini-scarf 0° and labeled MS0 (Figure 1-a), is a butt bonding of two parallelepipedic substrates with a square cross-section of 6 mm by 6 mm. The

theoretical bonded joint thickness is 0.4 mm. The volume to be investigated by X-ray tomography is located on both sides of the bonded joint and is represented in Figure 1-a by the parallelepiped ABCDHEFG. The MS0 configuration allows applying loading of tensile type since its direction remains perpendicular to the plane of the joint. The second configuration is referenced mini-scarf 45° and is hereafter labeled MS45. The particularity of this configuration is that the bonded joint is inclined at 45° with respect to the loading direction, thus allowing a proportional tensile–shear loading. The volume to be investigated by X-ray tomography is also shown in Figure 1-b and bounded by the parallelepiped ABCDHEFG. The 2017A aluminum alloy substrates that are used to prepare the samples have an M3 threaded end, allowing the sample to be fixed and mechanically loaded during the tomographic test. The mechanical properties of this aluminum alloy are as follows: Young's modulus E = 69 GPa and Poisson's ratio ν = 0.33. The experimental setup that allows the manufacturing of simultaneously several mini-scarf samples is shown in Figure 1-c. This bonding device allows for imposing the thickness of the joint by using appropriate wedges.

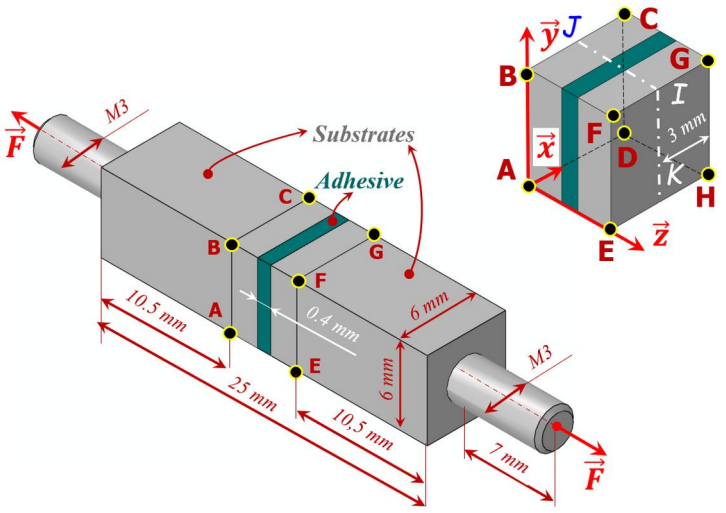

a)

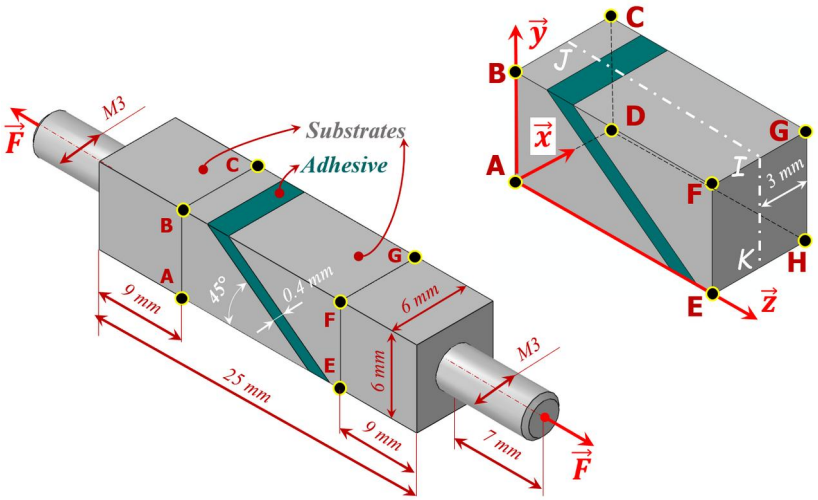

b)

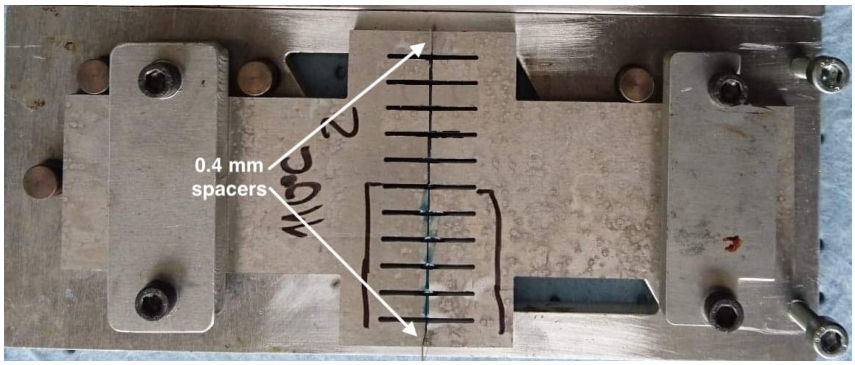

c)

Figure 1- Mini Scarf geometries for *in-situ* tomography applications. a) - MS0 bonding configuration (tensile loading); b) MS45 bonding configuration (proportional tensile-shear loading); c) – bonding device for manufacturing samples. More details on how this device works can be found in [21]

The surfaces to be bonded are treated following a standard procedure to guarantee the best adhesion properties possible. This treatment sequentially includes a first acetone cleaning, grinding with grade 180 sandpaper, and a final acetone cleaning. These steps remove the greasy impurities and oxide layers possibly formed during the machining, storage, and handling of the substrates.

The samples are bonded using an epoxy adhesive (*Huntsman™Araldite®* 420 A/B), cured at 110°C for 1h10. Araldite 420 A/B is a structural two-component epoxy adhesive produced by Huntsman, with a Bisphenol A diglycidyl ether prepolymer and a diamine

hardener mixed in stoichiometric conditions. The resin contains glass beads with diameters ranging from 30 µm to 70 µm, with a density of around 16 beads per mm^3. The role of these beads is to ensure the minimum thickness of the joint thus formed. It was checked by Differential Scanning Calorimetry (DSC) analysis that this cycle yields a fully polymerized material. Additional details regarding the surface preparation, the temperature control during the curing cycle, among others, can be found in the article [7].

2.2 *In-situ* X-ray tomography

As mentioned in the introduction, X-ray microtomography allows for the reconstruction and visualization of the internal structure of a visually opaque material. This non-destructive technique is based on the attenuation of X-rays during their propagation in a given medium. X-ray attenuation radiographs are gathered while rotating the sample to change the viewing angle. It is then possible from this full set of radiographs to reconstruct the observed volume, using various possible methods [24]. More extensive information regarding this technique and its application to the field of materials science can be found in the works of Kak [24], Dumont [19, 21], and Buffière [9] for instance.

A Phoenix VtomeX laboratory tomograph, which contains a Varian Paxscan X-ray detector with a resolution of 1920 x 1536 pixels was used. This detector produces radiograms of the attenuation, in gray levels coded on 16 bits. The samples described in the previous section are installed in a small electro-mechanical tensile machine placed within the chamber of the tomograph (Figure 2). This machine enables the application of a mechanical load to the tested specimens, in order to perform *in-situ* microtomography.

The voxel size obtained in the present configuration is 4.5 µm x 4.5 µm x 4.5 µm, which is suitable for the expected typical pore size. The data acquisition is performed for 1200 angular positions, for a total duration of about 12 minutes, an exposure time of 500 ms for each projection, and an X-ray source operating with a voltage of 80 kV and a current of 280 µA. The size of the reconstructed volume is 1500 x 1500 x 500 $voxels^3$, which corresponds to a volume of 6.8 x 6.8 x 6.8 mm^3. Figure 3 shows the results along the path JIK, as illustrated in Figure 1. This path represents a plane that intersects the

reconstructed volume in the middle plane of the sample, for both the MS0 and MS45 samples. The X-ray propagating direction is parallel to the $\vec{y}$ one (see Figure 1). In the MS0 configuration, the X-rays pass only through the bonded joint without being disturbed by the aluminum substrates, conversely to the MS45 configuration. The quality of the reconstructed volumes, in terms of signal-to-noise ratio, is then better for the MS0 than for the MS45 configuration. Yet the images are sufficiently good to allow the analysis of the MS45 sample.

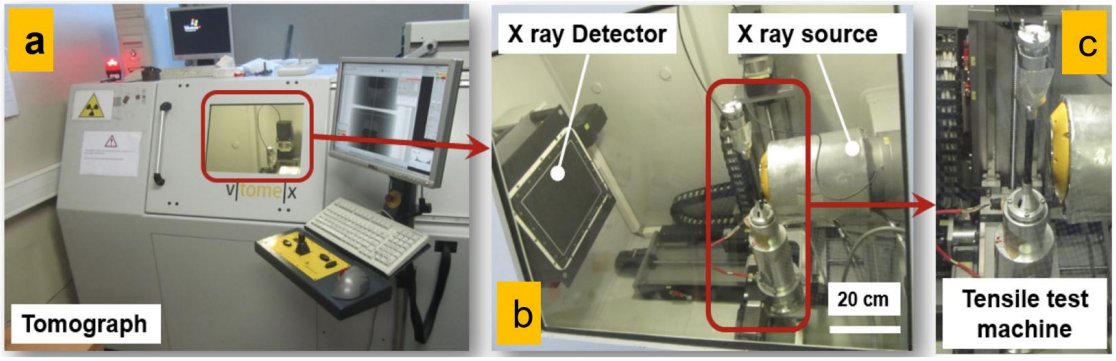

Figure 2: Experimental set-up a) general view, b) view of the inside of the tomograph, and c) close-up view of the tensile machine mounted on the rotating stage.

The mechanical loading procedure of these two bonding configurations is shown in Figure 4 and is of an interrupted multi-step type. This latter is generated by the traction machine located in the tomograph chamber (Figure 2). The loading from one step to another is controlled with a displacement speed of 0.5 mm/min up to a set force level. Once this force is reached, the displacement of the crosshead of the machine is blocked. Seven loading steps were applied to the samples MS0 and MS45.

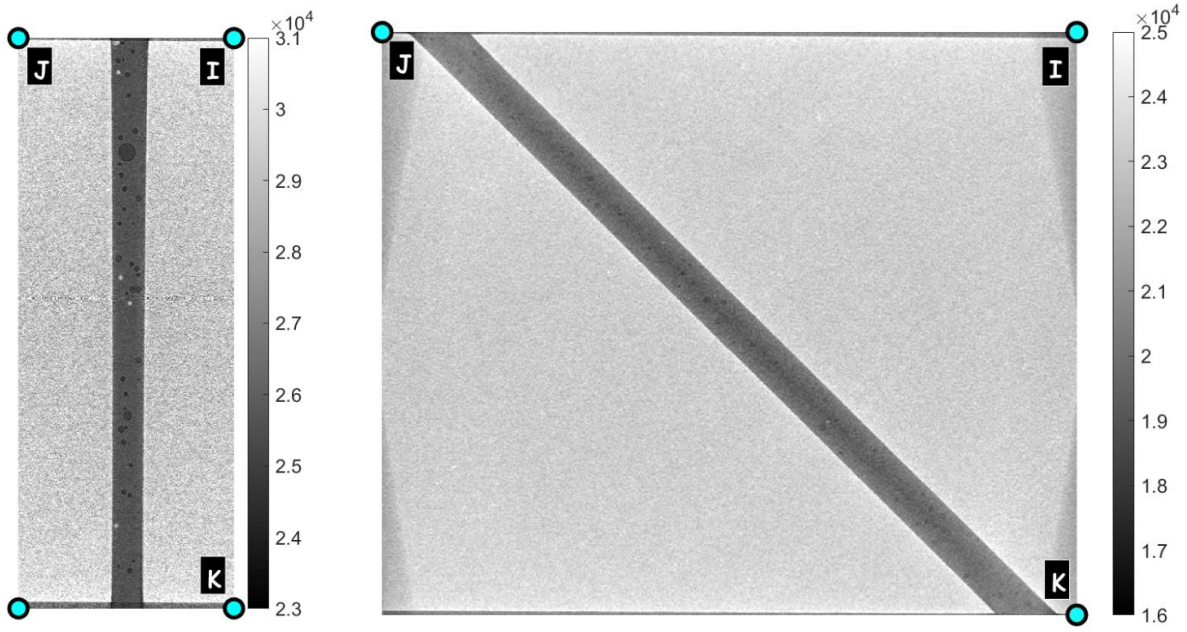

a) b)

Figure 3 – Mid-plane section (JIK) of each reconstructed volume of the sample. The color bar represents the gray levels on 16 bits: a) MS0; b) MS45.

It should be noted that a short stabilization time was waited before launching the acquisition for each step (Figure 4), in order to avoid any parasitic relaxation, a motion whose characteristic time would be significantly smaller than that of the tomography measurement, leading to blurry reconstructed data.

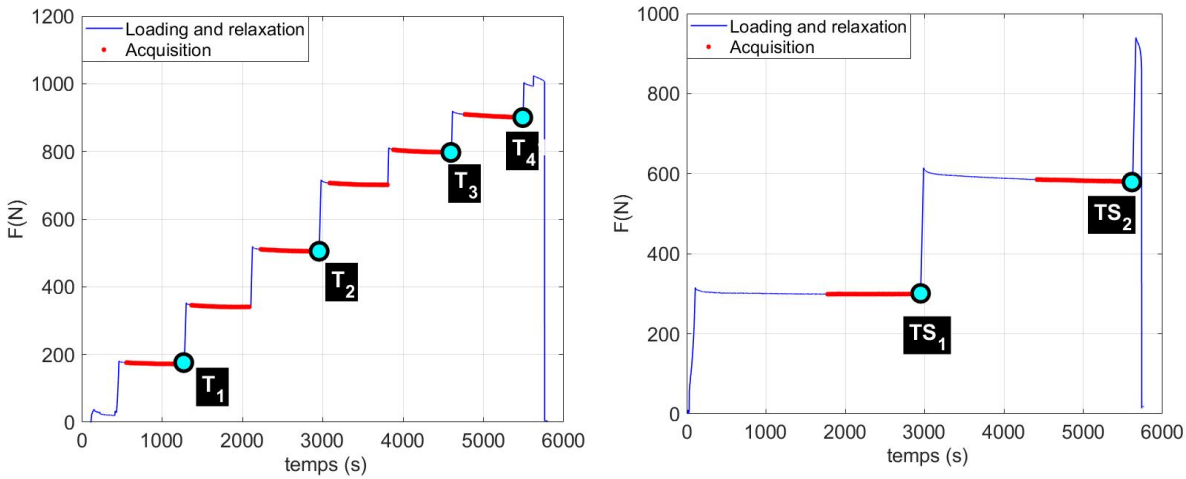

a) b)

Figure 4 – Mechanical loading applied to scarf samples: a) – loading procedure on

MS0 sample; b) loading procedure on MS45 sample

Six volumes were acquired from the MS0 sample and 2 from the MS45 one. However, a complete analysis of the volumic displacement fields was carried out during loading steps T_1, T_2, T_3, and T_4 on the MS0 sample and steps TS_1 and TS_2 on the MS45 sample.

3 Data processing

3.1 General principle

The processing of the data is divided into two steps. Firstly, the data must be segmented in order to isolate the pores from the remainder of the volume. This segmentation step, coupled with connected components analysis, allows for the extraction of various pore-related quantities, such as their equivalent diameter, and their spatial location, *among others*. Secondly, it is necessary to individually track each segmented pore throughout the complete mechanical test, to compute its displacement with respect to the applied load. The pore-tracking methods used in this work and the strategy for determining the volume displacement field are presented in section 3.3.

3.2 Segmentation

The data obtained from the tomographic measurements are greyscale reconstructed volumes of the samples (substrates, adhesive, and pores) and of the ambient air surrounding the samples in the tomograph. It is then mandatory to sort the voxels depending on the medium (*i.e.* aluminum, adhesive, or air). This step is known as *image segmentation* and is fairly common in image processing studies. A large variety of methods can be found to answer this particular issue, either based on greyscale thresholds [25], or other quantities as in the watershed algorithm [26, 27] and region-growing algorithms [28]. Figure 5 shows the histogram of the gray levels after filtering the tomographic data.

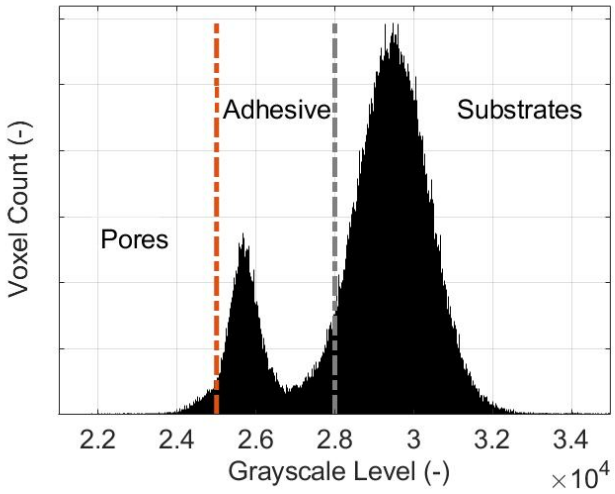

Figure 5 – Histogram of the reconstructed data for the MS0 bonding configuration and the computed thresholding levels for each phase: pores, adhesive, and substrates

Due to the shape of the histogram of the reconstructed volumes (Figure 5), it was chosen to use threshold-based processing. A generalized version of the approach proposed by Otsu [29] was used, to compute the two thresholds required to segment these trimodal data. Briefly, Otsu demonstrates in his paper that it is possible to compute an optimal threshold for segmenting bimodal by maximizing the interclass variance of the gray levels in each class. However, this approach must be generalized to a threshold number N_{thr} greater than one since Figure 5 shows a trimodal histogram. Otsu suggests that it is easily achievable by defining the discriminant criterion to be selected for optimizing the threshold values [15], and on which there are no restrictions on N_{thr}. In this study, a multi-threshold process is used for $N_{thr}=2$ in order to discriminate the following phases: the pores and the surrounding air within the tomographic chamber, the adhesive matrix, and the substrates.

To decrease the measurement noise on the reconstructed data, a contour-preserving 3D median filter [30] was applied prior to thresholding with a kernel size of 5 voxels. This segmentation technique is based on the works presented in [19, 21]. Some processing specifics had to be applied for the tomographic data associated with the MS45 bonding

configuration. Due to the relatively low contrast between the adhesive and the pores (Figure 3 – b), a 3D median filter of 7 voxels was applied to reduce the noise impact on the segmentation quality of the pores. In addition, the average gray level was homogenized since it exhibits relatively large variations in the vicinity of the substrates. This homogenization procedure of the substrates is explained in detail in [20]. The results of this segmentation procedure are shown in Figure 6. It is clearly visible that the proposed segmentation procedure leads to a conclusive separation of the different phases. Figure 6-a shows the tomographic data in the middle plane section (delimited by JIK in Figure 1-a) of the segmented volume that is associated with the MS0 configuration. In this figure, the adhesive is represented in black. and the pores appear as white spots. Figure 6-b shows the tomographic data in the middle section of the segmented volume that is associated with the bonding configuration MS45. Despite a very low contrast between the adhesive and the pores, the segmentation procedure is proving to be robust. The effect of noise on the segmentation quality, more visible in this MS45 configuration, remains acceptable, allowing us to efficiently separate the pores. As expected, the segmentation quality will affect the uncertainty of the displacement field. The pores with an equivalent diameter less or equal to two times the core size of the 3D median filter (i.e. 0.01 mm for the MS0 configuration and 0.014 mm for the MS45 one) are not included in the analysis since their detection is too much influenced by the noise level.

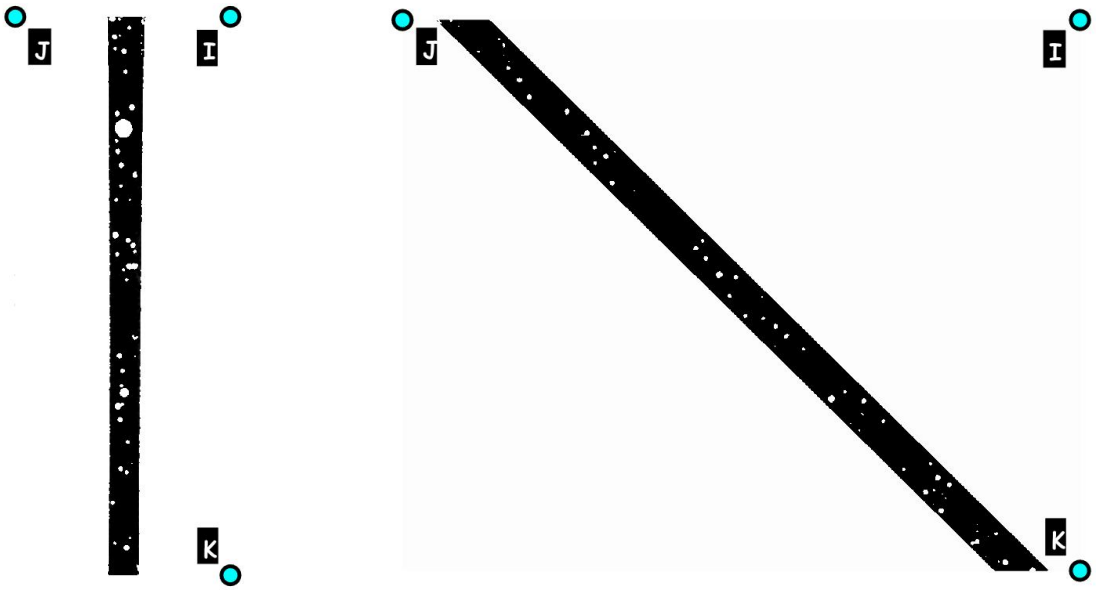

a) b)

Figure 6 – Tomographic data in the middle plane section JIK of the segmented volume a) associated with the MS0 bonding configuration; b) – associated with the MS45 bonding configuration

Using the Fiji software [31], Figure 7 shows a 3D visualization of the distribution of the segmented pores for both configurations MS0 and MS45. This representation allows stating, firstly and qualitatively, that the distribution of the rather spherical pores remains relatively homogeneous. The volume fraction of voids, after the polymerization cycle is approximately 1.63%.

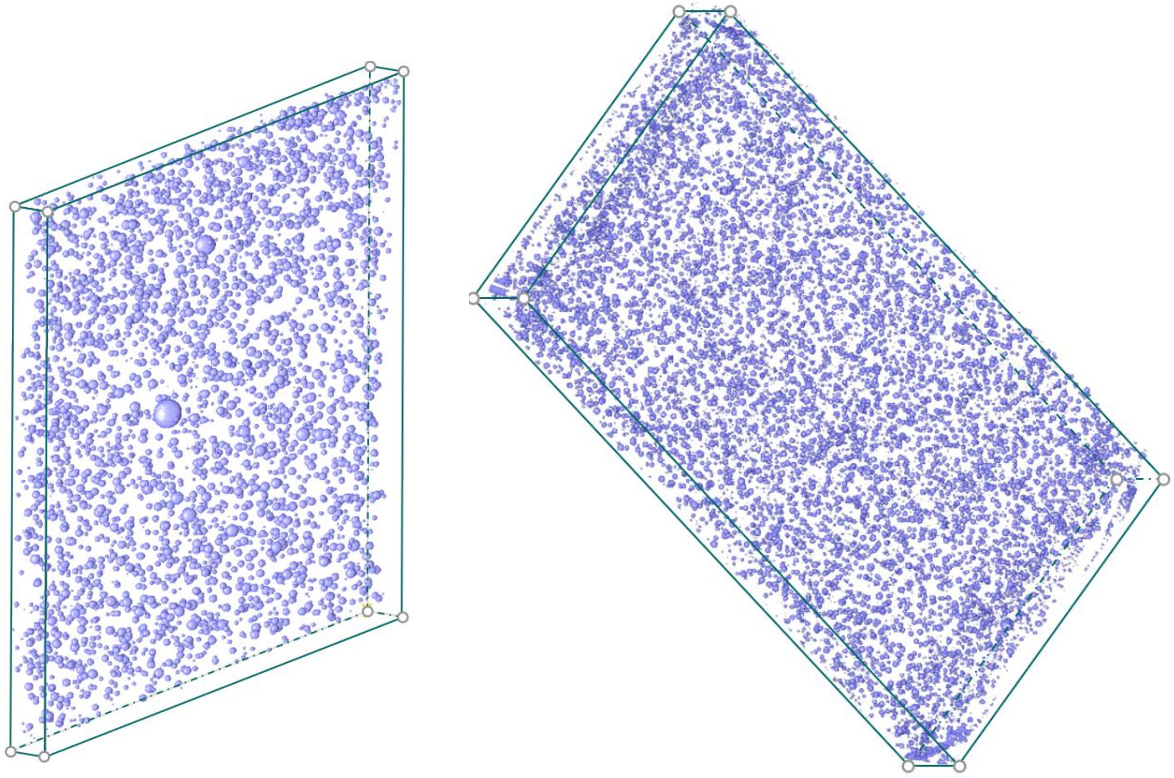

a) b)

Figure 7 – 3D visualization of the distribution of pores within the initial state of the adhesive volume a) – associated with the MS0 bonding configuration; b) – associated with the MS45 bonding configuration

The presence and morphology of the pores within this adhesive are mainly due to two fundamental mechanisms: i) the mixing of the two components of the adhesive (matrix and hardener) generates the first population of pores. These latter are generated by the glass beads characterized by an average size of 75 µm and in motion during this mixing. ii) then, the polymerization cycle also modifies the pore size. More precisely, it was noticed that the pore size increases with the curing temperature. More details on the pore origin are given in [19]. Figure 7-a shows the presence of a pore with a relatively large size, which is due to trapped air during the manual process of adhesive spreading on the substrates. In the case of the MS45 bonding configuration, Figure 7-a shows a relatively homogeneous pore distribution, with however some segmentation artifacts in the vicinity of the joint edges (those close to the points J and K in Figure 6-b. Since the pore shape is rather spherical, an equivalent diameter can be associated with their

geometry. In the case of the MS0 bonding configuration, Figure 8-a shows the diameter distribution in the initial state of the joint and when this latter is subjected to a loading force of 900 N (final state). For each of these two states, the diameter distribution seems rather of a Gaussian type characterized by a mean of 0.049 mm for the initial state and 0.052 mm for the final one. This finding is of great importance since it highlights that the equivalent pore diameter is only weakly influenced by mechanical loading. To better understand the evolution of the geometry shape, the evolution of the pore sphericity is plotted as a function of the corresponding equivalent diameter (Figure 8-b). From this plot, one can observe that between initial and final states, the pore shape evolution is almost undetectable. Therefore, one can make the hypothesis that the pores behave as quasi-rigid markers, and their small change in shape and volume will only slightly affect the measurement of the volumetric displacement field; this measurement being based on the position of the pore centroids.

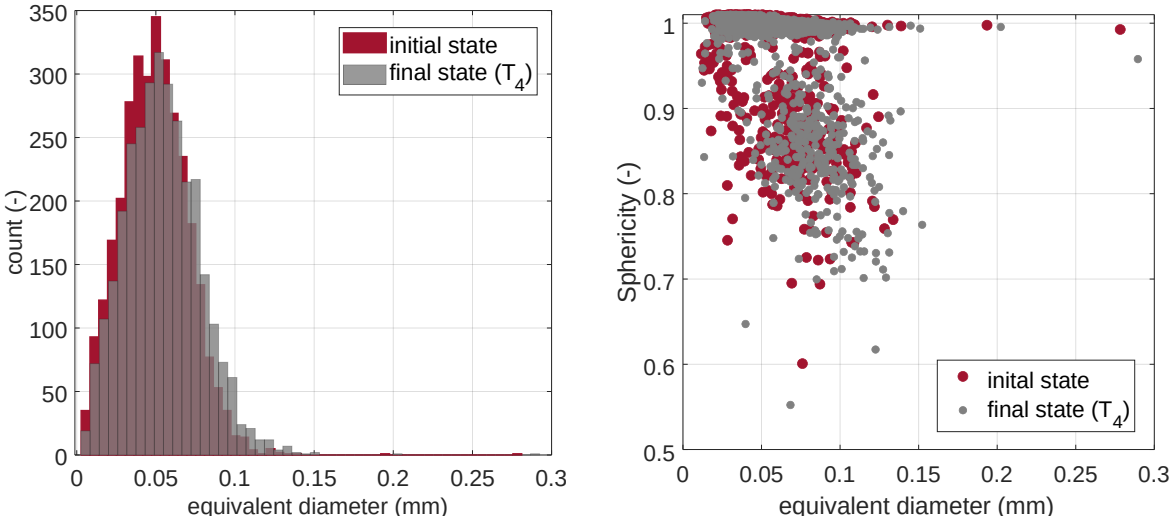

a) b)

Figure 8 – MS0 bonding configuration: histogram of pore distribution in both the initial and final state of the adhesive. a) –distributions of pore equivalent diameter; b) – distributions of pore sphericity as a function of its corresponding equivalent diameter

The pores, selected as markers, will allow the monitoring of the joint displacement field. The density of this latter is thus directly correlated with the pore one. The computation of the volumetric displacement field of the adhesive is given by the following formula (Eq.1) :

$$\vec{u}_{pi} = \vec{d}_{p_i^f} - \vec{d}_{p_i^o} \quad \text{Eq. 1}$$

Where $\vec{u}_{pi}$ represents the 3D displacement of the pore p_i, $\vec{d}_{p_i^f}$ represents the position vector of the pore p_i barycentre in cartesian coordinates in the deformed state, and $\vec{d}_{p_i^o}$ represents the position vector of the pore p_i barycentre in cartesian coordinates in the initial state.

Thus, it is of great importance that the pores be segmented using robust strategies since the position of the barycenter strongly influences the computation of the displacement field. The detection of the rotation of the pore p_i is not investigated in this study because the quasi-spherical shape of the pores precludes such a measurement. The main challenge is thus to find the right correspondence of the pore p_i in each adhesive loading state. The following section describes three methods that allow tracking the pore positions in each deformed adhesive state.

3.3 Pore tracking methods

The experimental measurement of the volume displacement field has been addressed in numerous works [32, 33] based on the principle of Digital Volume Correlation (DVC). However, in our case, given the low pore density compared with optimal volume coding [33] used in DVC, this method is not appropriate. So, to get around this problem and move towards particle tracking instead, it will enable us to obtain a more localized volume displacement field compared with DVC. This issue has already been investigated in numerous works [34, 35, 36, 11]. The approach proposed in this study is mainly based

on marker tracking and particle imaging velocimetry (PIV) techniques. The objective here is to propose a strategy that is both robust and fast, allowing thus an automatic computation of the displacement field for a considerable number of loading states. The first strategy proposed is called the **Step-by-Step Approach** (**SSA**) method. The second one called the **Identity Indicator Label (IIL)** method, is mainly based on the ID-Track approach described in [34] and adapted to this study. The general idea is to propose an identity card for each pore, and this indicator must be unique allowing thus to find the correspondence between the pores for different loading states. The third and last strategy called the **Pore Correlation** (**PCORR**) method aims at finding the pore position by determining a correlation coefficient between a segmented sub-volume surrounding the pore p_i in the deformed configuration and the initial segmented volume. In the following sections, each method will be briefly described while specifying its advantages and disadvantages. It is important to specify that once the pores are segmented, preliminary processing is required to identify data that are essential for the measurement of the displacement field. First, each pore type is selected and their number as a function of the adhesive loading state is evaluated as well as its barycentre, outer surface, volume, and sphericity, among others. The algorithms that are used in the preliminary process are described in more detail in [37].

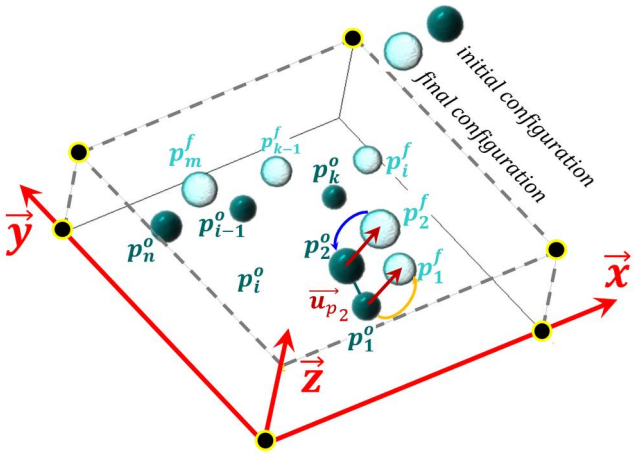

Figure 9 – Principle of Step-by-Step Approach (SSA) method

3.3.1 Step-by-Step Approach (SSA) method

This approach has the advantage of being very simple and having low computational time. Its principle is shown in Figure 9 and is broken down into five steps.

First, the segmented pores are identified in both adhesive states: initial and final, and p_i^o and p_i^f are the labels of the same pore p_i in these states. The label is an integer that varies between 1 and the maximum number of pores in the analyzed adhesive state. All the voxels associated with the same pore have the same label. If a voxel is not associated with a pore, its label is zero.

In the second step, the algorithm is initialized by specifying manually the correspondence that seems obvious between two pores (often a pore of great size, easily detectable with the naked eye through a simple observation of these two adhesive states). For example, in Figure 9, it is imposed that the pore p_2^o of the initial state corresponds to the pore p_2^f of the final state.

In the third step, the volumetric displacement field $\vec{u}_{p2}$ of the pore is computed using Eq.1.

In the fourth step, we look for in the final state the closest pore of the pore p_2^f. In the case represented in Figure 9, this is the pore p_1^fthat corresponds to p_1^0 in the initial state. To find out the label of the pore p_1^f it is supposed that its displacement $\vec{u}_{p1}$ is close to that of the pore p_2^f , so $\vec{u}_{p2}$. Thus, the label of the pore p_1^f in the final state is that of the voxel in the position given by the vector $\vec{d}_{p_1^{\square}}$. This latter is evaluated as follows:

$$\vec{d}_{p_1^{\square}} = \vec{d}_{p_1^o} + \vec{u}_{p2} \qquad \text{Eq. 2}$$

Where the vector $\overrightarrow{d_{p_1^o}}$ represents the cartesian coordinates of the barycentre of the pore p_1 in the initial state and $\overrightarrow{u_{p2}}$ represents the pore displacement for which its correspondence in the initial state has been imposed (step 2 of the algorithm).

The fifth step consists in looking for the closest pore to the pore p_1 that has not yet been matched and repeat steps three and four. The fifth step must be repeated until all pores have found their correspondent in the final state. Once all the correspondences are found, the displacement field is computed using (Eq.1).

3.3.2 Identity Indicator Label (IIL) method

This second method aims to find an identity indicator and label each pore. Moreover, one wishes that this indicator be a scalar specific for each pore and that it changes little, if any, for a pore being in different loading states. So first of all, some assumptions are made: i) the geometric shape of the pore changes very little, ii) the position of the neighboring pores to the pore p_i remains relatively stable, and iii) the volume of each pore is only evolving very slightly. Then, for each pore p_i we associate an identity indicator C_i^{config} that is composed of several parameters specific to the pores and is expressed as follows (Eq. 3):

$$C_i^{config} = \alpha\sqrt{x_i^2 + y_i^2 + z_i^2} + \beta V_i + \gamma \Psi_i + \delta \sum_{j=1}^{k} d_j \quad \text{Eq. 3}$$

where x_i, y_i, and z_i represent the cartesian coordinates of the barycentre of the pore p_i, V_i represents its volume, and Ψ_i its sphericity. $\sum_{j=1}^{k} d_j$ represents the sum of distances d_j between the pore p_i and the k nearest pores. α, β, γ, and δ are weighting coefficients.

The sphericity is thus computed using the formula (Eq.4) proposed by Wadell [38]: where A_i represents the external surface of the pore p_i.

$$\Psi_i = \frac{\pi^{\frac{1}{3}} \left(6 V_i\right)^{\frac{2}{3}}}{A_i} \qquad \text{Eq. 4}$$

The superscript of the indicator C_i^{config} can take the values 0 or *f*, representing the initial or the final configuration, respectively. Figure 10 shows a schematic representation of the concept of this method applied to two configurations. A vector containing ***n*** identity indicators $C^o_{i\epsilon[1,\ldots,n]}$ is calculated for the initial configuration and another vector containing ***m*** identity indicators $C^f_{i\epsilon[1,\ldots,m]}$ for the final configuration. One calculates the correlation matrix C_{hl}^{corr} using the formula (Eq.5) with $h\epsilon\left[1,\ldots,n\right]$ and $l\epsilon\left[1,\ldots,m\right]$.

$$C_{hl}^{corr} = \left|\left[C_h^o - C_l^f\right]\right| \qquad \text{Eq. 5}$$

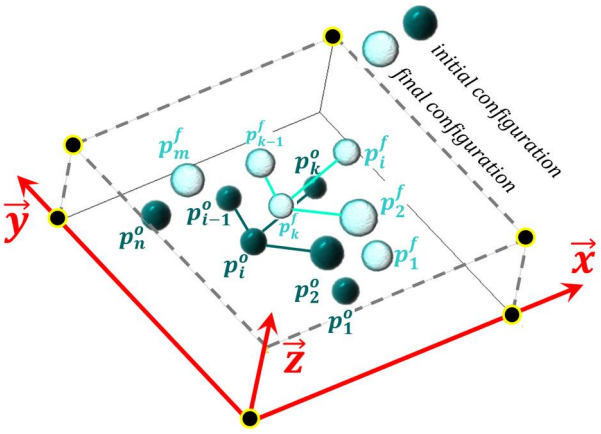

Figure 10 - Principle of Identity Indicator Label method (IIL)

3.3.3 Pore Correlation method - PCORR

The objective of this third method is to find the pore correspondence between two configurations based on coupling the label of these pores to the positions $\vec{d}_{p_i^0}$ and $\vec{d}_{p_i^f}$. These latter represent the positions of the barycenter of pore p_i in the initial and final configuration. Once this match has been found, the displacement is calculated using the

expression (Eq.1). In concrete terms, to find the correspondence, we generally try to evaluate the vector $\vec{d}_{p_i^f}=\vec{d}_{p_i^0}+\vec{u}_{pi}$, where $\vec{u}_{pi}$ represents the displacement in voxels of the pore p_i. This displacement is expressed in the form $\vec{u}_{pi}=u_x\vec{x}+u_y\vec{y}+u_z\vec{z}$ and is mainly based on the concept of digital volume correlation [39]. This concept is however adapted and simplified (see Figure 11-a) in our study by evaluating first and separately the displacements $u_x\vec{x}$ and $u_y\vec{y}$ in $\vec{x}$ and $\vec{y}$ directions and then $u_z\vec{z}$ in $\vec{z}$ direction. This macro-displacement (because of no sub-voxel resolution) is computed through the following steps: the first one transforms the segmented volumes of the two pore configurations (initial and deformed) into two images, representing the average of all voxels in the $\vec{z}$ direction. These two images are shown (Figures 11-b) and c). In the second step, the two previous images are used to compute the macro-displacement $u_x\vec{x}$ and $u_y\vec{y}$ in the $\vec{x}$ and $\vec{y}$ directions. Then iteratively, for each pore p_i^o in the initial configuration, we define for it, in the plane $\vec{x}o\vec{y}$ and around its barycenter, a square-shaped zone of interest (ZOI) and side l_{ZOI} (figure 11-b). The value of the l_{ZOI} parameter must be large enough to include at least 5 pores so that the correct position of the pore in the plane $\vec{x}o\vec{y}$ can be found with less uncertainty. Next, another region of interest (ROI) will be defined, square in shape and centered on the pore position and side $l_{ROI}=2\times l_{ZOI}$. This ROI will be positioned on the image of the final configuration as shown in Figure 11-c. To evaluate the macro displacement, the zero-mean normalized correlation coefficient (ZNCC) map in 2D through the convolution between ZOI and ROI. The maximum value of this map allows us to evaluate the macro displacements u_x and u_y . The final stage aims to find the macro displacement u_z of the pore $p_i^{\square}$ in the $\vec{z}$ direction. A ZNCC correlation coefficient was computed, in 1D, between the grey level (here, voxels have binary values 0 and 1) of a line (defined by the vector $\vec{d}_{p_i^0}$ in the initial configuration) parallel to the $\vec{z}$ direction and that crosses the pore at its barycenter and the grey level of a second line (in the final configuration) parallel to the $\vec{z}$ direction and defined by the partial position (since only u_x and u_y are known) of the barycenter determined in the previous step. The maximum value of this correlation coefficient

allows us to compute the $u_z\vec{z}$ displacement and complete the coordinates of the vector $\vec{d}_{p_i^f}$. This method is considered more robust than the previous two, as it is not influenced by the presence of pores appearing only in the final configuration. Moreover, this method opens up an interesting prospect, enabling us to highlight pore fusion or identify pores that appear during mechanical loading, as already demonstrated at the global scale of the joint [20].

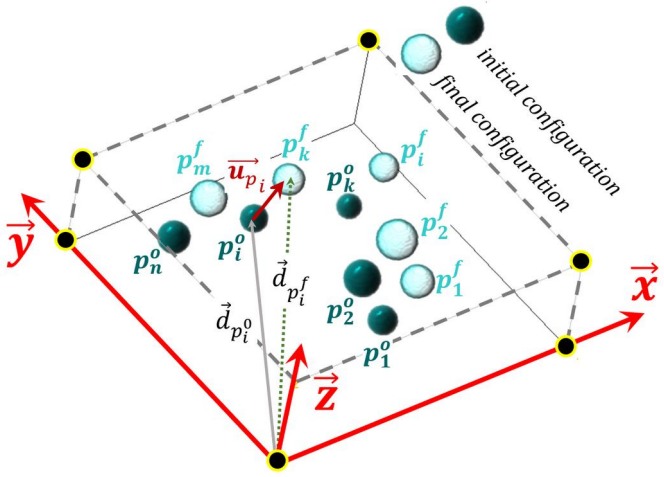

a)

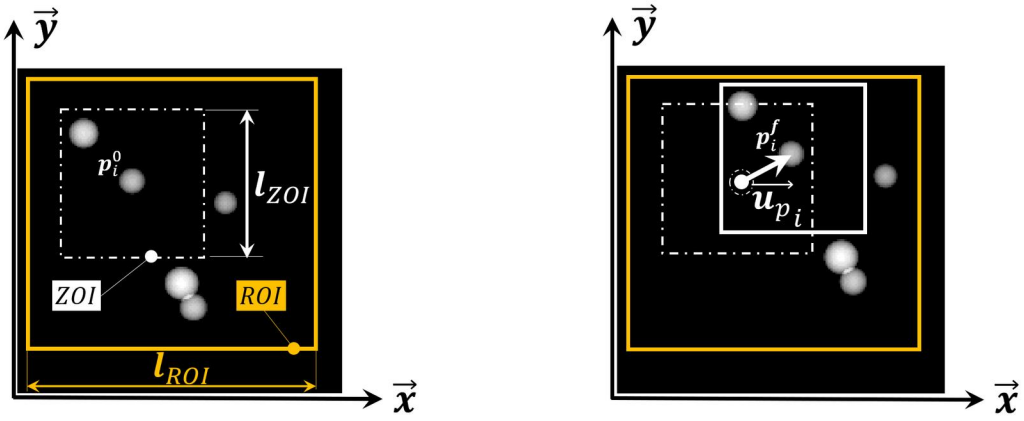

b) c)

Figure 11- Principle of the Pore Correlation method**.** a) **–** Initial and final configurations of the segmented volume; b) – mean of the segmented volume in the initial configuration in the $\vec{z}$ direction; c) mean of the segmented volume in the final configuration in the $\vec{z}$ direction.

To discriminate the three proposed methods, and thus determine their ability to track pores through different configurations and scenarios (opening mechanisms, coalescence, among others.), it is necessary to carry out a study on synthetic volumes for which the displacement field, pore distribution, noise measurement, among others, are already known. The following section will develop this very important aspect, as it enables one to choose the most appropriate method for a given scenario.

4 Study on artificial tomographic datasets

The purpose of the synthetic tomographic volume is to characterize and discriminate between the three proposed methods, and to examine their behavior in more detail under several parameters such as measurement noise, voxelization, the contrast between adhesive and pores, and minimum distance between pores.

4.1 Construction of the numerically generated test volumes

The construction of such a test volume is based primarily on the characteristics observed in the actual volumes determined in this study. More precisely, the synthetic volume generated corresponds to the initial state for a pore distribution similar to that shown in Figure 8-a in terms of size, number of pores, equivalent diameters, porosity rate, the minimum distance between pores, as well as measurement noise. The only difference between synthetic and real volumes is that the pores of the synthetic volume will remain rigid and spherical (with no change in shape and volume). In practice, Figure 8 shows a very slight evolution in pore diameters and a change in sphericity. The detailed construction of such a volume and all its specific characteristics can be found in [20]. This volume is shown in Figure 12-a.

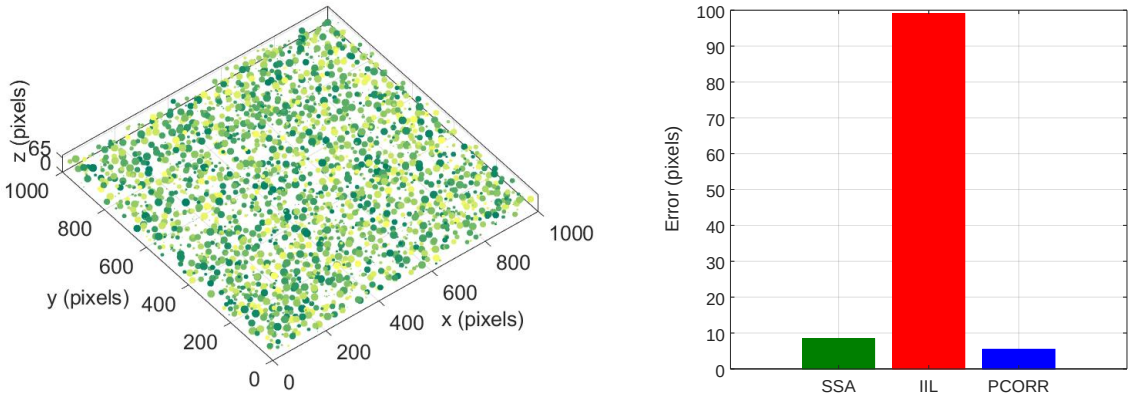

a) b)

Figure 12 – Synthetic volume and comparison between the three pore tracking methods. a) – Spatial distribution of rigid pores in the synthetic volume; b) – Comparision between the three methods

From the initial volume generated as explained above, a second synthetic volume is constructed by applying a displacement field, here only in the $\vec{x}$ direction, to all the pores of the initial volume following the formula described in (Eq.6). A maximum displacement of 3 pixels was applied, a value consistent with the order of magnitude of the displacement found on mini-scarf samples, but also motivated by the fact that we want all the pores in the initial configuration to be in the final one (here, no pore fusion, or pores that are only in the final configuration). The three methods (SSA, IIL, and PCORR) were then used to track the pores for initial to deformed states.

$$\overrightarrow{u_p(x)} = u_{x_{the_i}}(x)\vec{x}\,;\, u_{x_{the_i}} = 3 \times \frac{x^2}{1000^2}(pixels) \qquad \text{Eq. 6}$$

The error associated with each method is calculated using the formula (Eq.7) where $u_{x_{the_i}}$ represents the theoretical displacement of the barycenter of each pore and $u_{x_{mes_i}}$ represents the measured displacement for the pore « i » using different methods.

$$Error = \sum_{i=1}^{n_p} \left| \left(u_{x_{the_i}} - u_{x_{mes_i}} \right) \right| (pixels) \quad \text{Eq. 7}$$

The result of the error in each of the three tracking methods is shown in Figure 12 b. Several parameters could influence the value of this error, such as measurement noise, mean intensity variation, phase contrast, and size of filters used to improve segmentation, among others. For a more pertinent comparison, only the contribution of the inevitable voxelization error was retained, and the one due to pore mismatches. It can be seen from Figure 12-b that the ILL method appears to be the least efficient since the error is at its maximum. This can be explained by the fact that there are some incorrect pore couplings because the identity indicators of different pores are very close to each other. On the other hand, the SSA and PCORR methods have relatively close errors. Only two mismatches were detected for the SSA method and none for the PCORR one. The error value from the PCORR method is close to zero and represents the voxelization error, which affects all pores regardless of the method used. This type of error will be discussed in detail in section 4.2. As an example, the superposition of the theoretical displacement field $u_{x_{the_i}}(x)$ with the measured displacement $u_{x_{mes_i}}(x)$ obtained with the PCORR method was plotted in Figure 13.

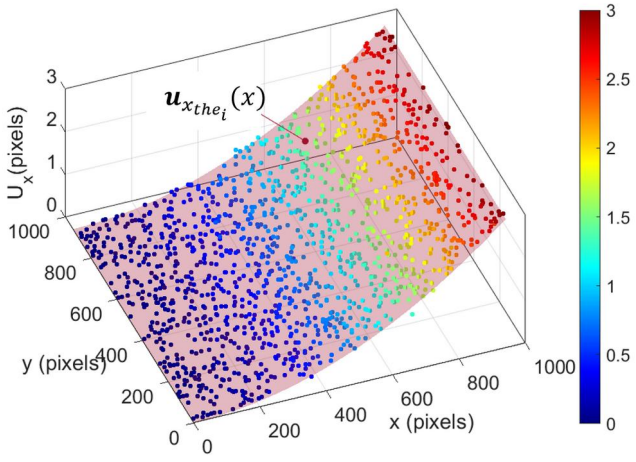

-

Figure 13 – Theoretical displacement field $u_{x_{the_i}}(x)$, depicted by the pink surface, *vs*.

measured displacement $u_{x_{mes_i}}(x)$, represented by the color-coded dots

Based on the results in Figure 12-b, we conclude that the most adaptable method in our study is the PCORR method. This method was used in the analysis of numerical and experimental data

4.2 Influence of the voxelization on the detected displacements

During acquisition and segmentation, continuous analytical objects (pores, inclusions, *among others*.) are transformed into discrete objects as a result of voxelization. This voxelization can have a significant influence on the calculated displacements, especially for small objects because the difference between continuous geometry and voxelated geometry is all the greater. In order to estimate this influence, it is proposed to consider elementary volumes containing a pore of variable diameter (*i.e.* of variable sensitivity to voxelization effects). To simulate the voxelization occurring during the tomographic measurement and segmentation process, an array M_{ijk} of dimensions *(x, y, z)* is built, whose elements *(i, j, k)* are defined by (Eq.8).

$$\begin{cases} M_{ijk}=1, \wedge \sqrt{(i-x_c)^2+(j-y_c)^2+(k-z_c)^2} \leq r_{por} \\ M_{ijk}=0, \wedge else \end{cases} \quad \text{Eq. 8}$$

As an example, the morphology of 4 voxelized spheres with radii of 3, 5, 10, and 20 voxels is shown in Figure 14. It can be clearly seen that the volume and consequently the barycenter of the sphere is affected in a significant way, as soon as the radius decreases.

with r_{por} the radius of the considered pore and (x_c, y_c, z_c) the coordinates of the barycenter of the pore. It should be noted that the characteristics of the pore are not necessarily integers (i.e. the quadruplet $(x_c, y_c, z_c, r_{por}) \in R^4$).

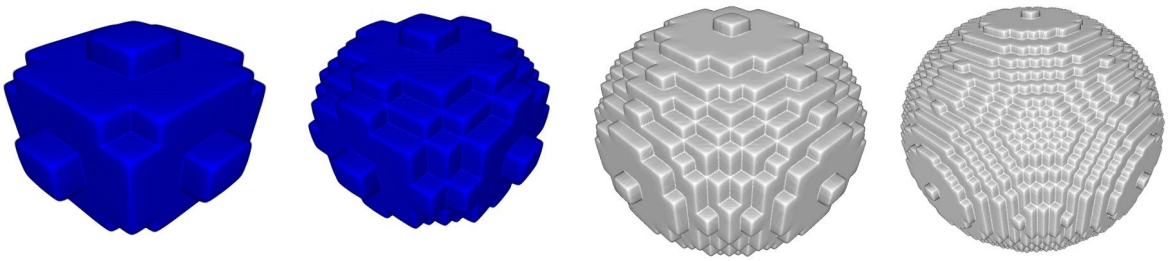

$r_{por} = 3\,voxels$ $r_{por} = 5\,voxels$ $r_{por} = 10\,voxels$ $r_{por} = 20\,voxels$

Figure 14 - The voxelization effect on a sphere of different radii

A displacement of 0.5 voxels is applied to (x_c, y_c, z_c) along three axes: $\vec{x}$, $\vec{y}$ and $\vec{z}$. This is the most critical case, as the effect of voxelization will affect all three directions simultaneously, enabling us to estimate the maximum error likely to occur during voxelization. Next, the voxelization process is applied again (Eq.8), to obtain a deformed volume. The post-processing presented above is finally applied to the initial and deformed volumes, to obtain a measured displacement to compare with the imposed displacement. The detection error ε is then calculated according to (Eq. 9).

¿ Eq. 9

with (x_c, y_c, z_c), $(x¿¿c', y_c', z_c')¿$ and $(x_{detect}, y_{detect}, z_{detect})$, the coordinates of the theoretical initial pore, the coordinates of the theoretical final pore, and the coordinates of the detected final pore respectively.

This comparison is made for a series of diameters distributed between 5 and 40 voxels, as shown in Figure 15.

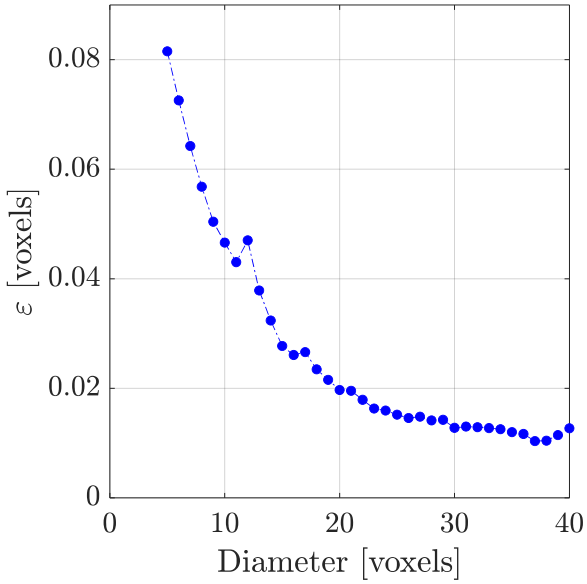

Figure 15 - Influence of the size of the pores and the voxelization on the error epsilon in the detected displacement

It should be noticed that for the minimum pore size considered afterward (V > 125 voxels, corresponding to a diameter of about 8 voxels), the error made on the determination of an imposed displacement of 0.5 voxels along tree axes is about 0.056 voxels, *i.e.* 6,4%

4.3 Influence of the measurement noise on the detected displacement

As already mentioned, the postprocessing performed on these tomographic data is relatively sensitive to the measurement noise, due to the properties of the employed tools (*i.e.* thresholding, mainly). Among other elements, an inhomogeneous (and therefore defective) detection of contours beyond a certain noise level can be expected. To estimate the influence of this parameter on the displacement detection capabilities, the approach presented above (generation of artificial pores, application of a known displacement to the synthetic representative elementary volume, calculation of displacement by tracking, and comparison with the imposed theoretical value) is

applied, for various noise levels. Each noise level is generated according to a Gaussian distribution, as suggested by the histograms obtained from the experimental data [20]. Each noise draw is therefore defined by the standard deviation of its distribution. However, the important parameter here is not the value of this standard deviation, but the value of the ratio $\eta = \frac{\sigma_b}{\Delta_{bgsl}}$ with σ_b being the standard deviation of the Gaussian noise distribution and Δ_{gsl} being the difference between the greyscale levels of the adhesive and the pores. The results are presented in Figure 16 – a.

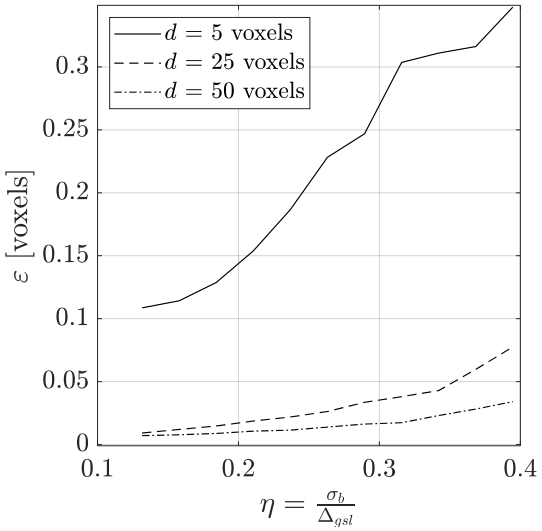

a) - Error committed on the detection of a 0.5 voxel displacement as a function of the noise level η and for various pore diameters (5, 25, and 50)

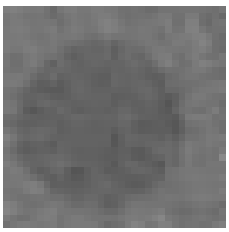

b) - Raw data with a high-intensity measurement noise ($\eta = 0.39$)

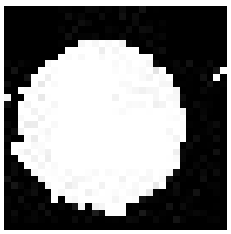

c) - Obtained segmentation

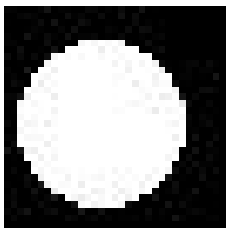

d) - Reference

Figure 16 - Influence of the measurement noise on the detected displacement

For information purposes, η = 0.3 for the actual experimental data. Except for the smallest pores for which there will be a high uncertainty, the displacements calculated for noise levels of this order of magnitude have small errors compared to the imposed displacements.

4.4 Detection of subvoxel displacements

According to the data presented in Figure 13, it appears that the developed tool is able to detect subvoxel displacements with rather good reliability, especially if the object to be considered is of sufficient size. It is therefore interesting to investigate the limits of the proposed methodology in terms of subvoxel displacements. As it may be seen in Figure 13, the diameter d of the pore used as a marker is an important factor; consequently, three different cases should be studied: a small pore (d = 5 voxels) as the first extreme case, a standard pore (d = 25 voxels) and a large pore (d = 50 voxels) as the second extreme case. The imposed subvoxel displacements are distributed between 10^{-3} voxel and 1 voxel, for the three proposed pore sizes.

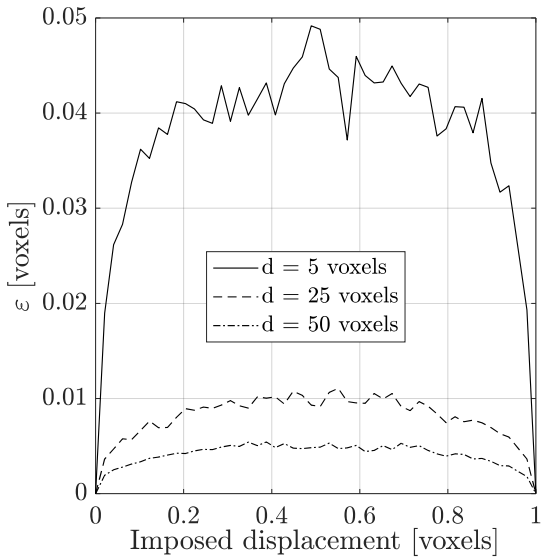

Figure 17: Influence of subvoxel displacements

The results of these calculations are presented in Figure 17. As suggested by the data displayed in Figure 16 – a), the larger the pore, the more reliable the displacement calculation. Moreover, in a rather intuitive way, the error ε hits its maximal value for an

imposed displacement of 0.5 voxel, in all three cases. In the worst case (r_{por} = 2.5 voxels, $d_{imposed}$ = 0.5 voxel), an error of roughly 10% on the detected displacement is obtained using the proposed tool.

5 Results

Given the results obtained previously, the most robust method appears to be the PCORR. In the remainder of this work, this method was only used and applied to experimental data from two configurations: MS0 and MS45. The processing of the raw tomographic data will not be detailed here, but the full strategy can be found in the article [21].

5.1 Scarf 0°

In the MS0 case, the stress state of the joint is close to a tensile state. Given the geometry in the vicinity of the joint's free edge, where very high-stress concentrations are generated, joint failure is expected to occur relatively early and at relatively low average stresses, compared with the adhesive's maximum failure stress. By way of example, the maximum tensile stress of this adhesive for this polymerization cycle is 48 MPa, while for the MS0 configuration, it is 27 MPa. In the following, the volume displacement fields for the four levels T_1, T_2, T_3, and T_4, we will show, first in the $\vec{x}$ and $\vec{y}$ directions (in the plane of the joint) and then the volume displacement in the $\vec{z}$ direction (out-of-plane) of the joint. 3197 pores could be detected in this configuration, giving a displacement measurement point density of around 222 pores per mm^3. The measurement resolution here is equal to the pore size, making this strategy capable of determining localized evolutions as a function of pore density.

5.1.1 In-plane displacement fields

The experimental displacement fields in the plane of the joint are shown in Figure 18. For each pore, its barycenter is represented in a Cartesian coordinate system A $\vec{x}$ $\vec{y}$ $\vec{z}$ (Figure 1-a), and the displacement associated with this point is represented by an appropriate color code. Rigid body motion has been eliminated to better represent the state of stress of the joint. Both displacement fields $u_x\vec{x}$ and $u_y\vec{y}$ are relatively similar

and consistent with the kinematics of the bonded joint. They exhibit increasingly large displacement values in the vicinity of the joint's free edge and perpendicular to the direction of investigation, reflecting the Poisson's effect. These displacements in the vicinity of the free edge move symmetrically toward the inside of the joint. It can also be seen that there are a few randomly distributed points, showing somewhat outliers.

	U_X (mm)	**U_Y (mm)**
T_1	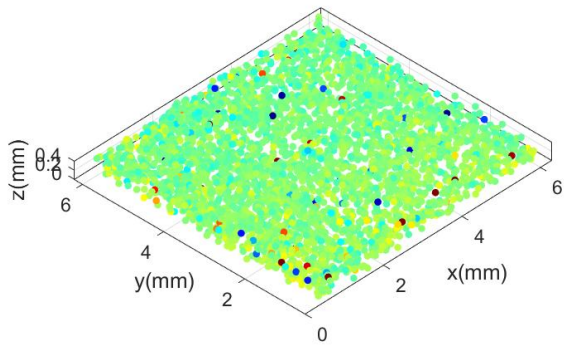	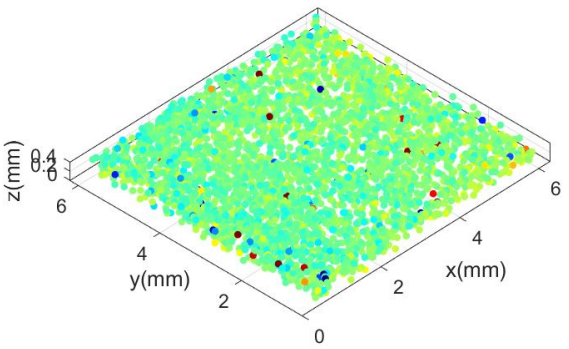
T_2	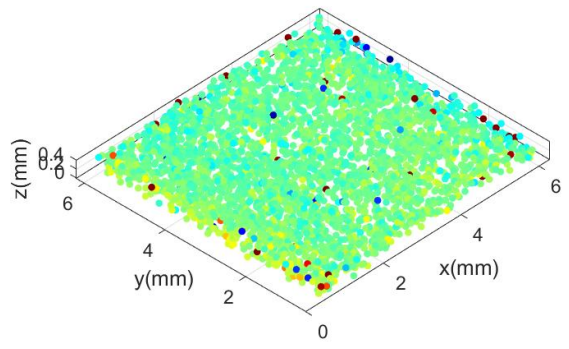	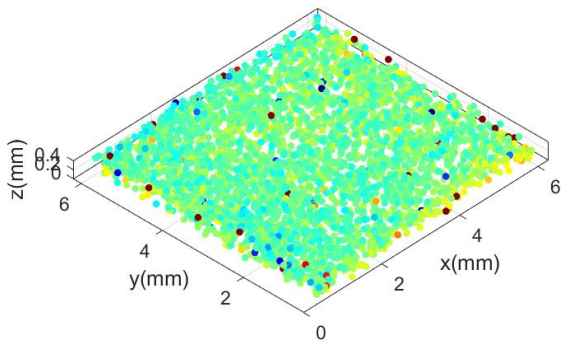

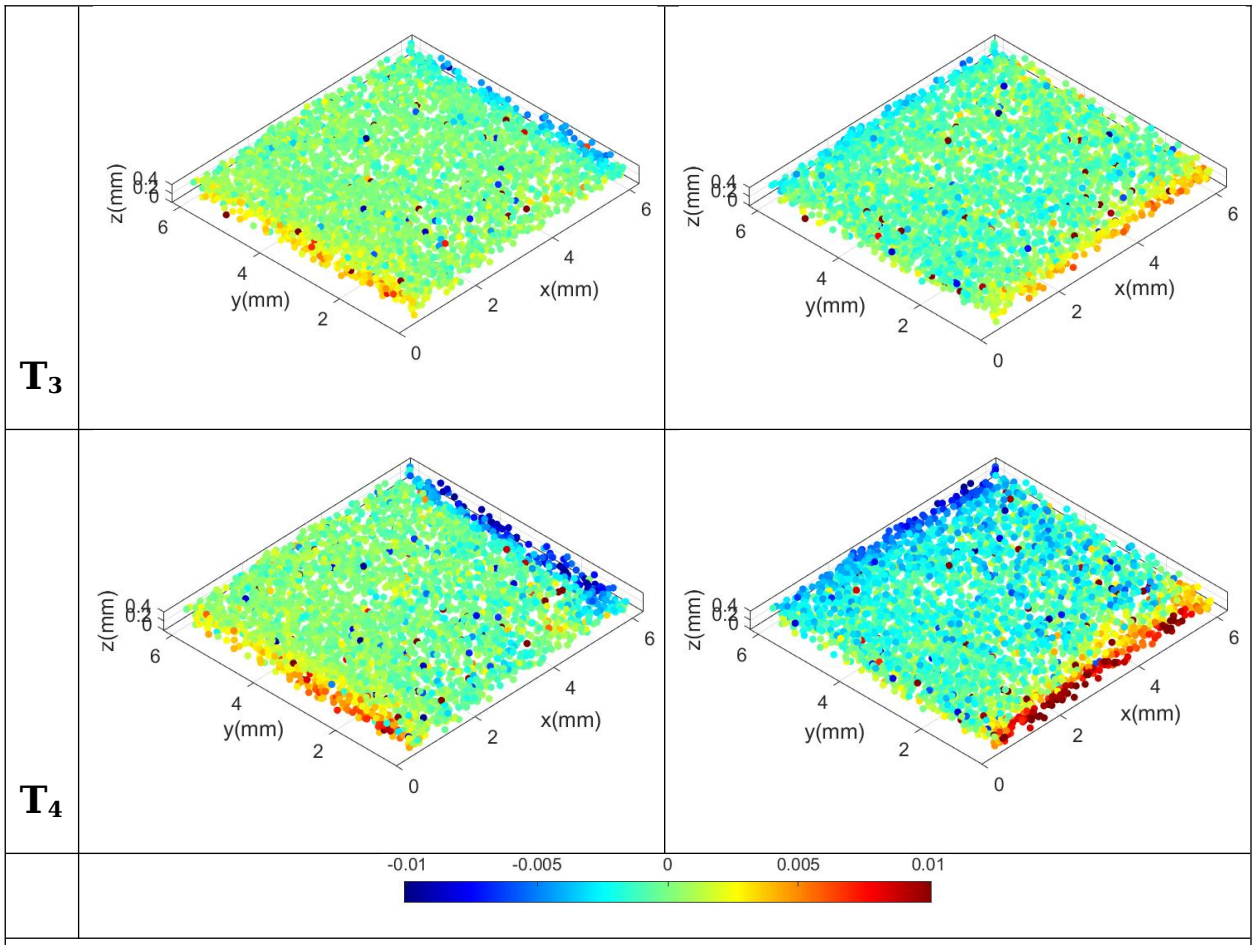

Figure 18 – u_x and u_y displacement fields [in mm] in the joint plane

This can be explained by a few very small pores (around 5 voxels in diameter) that are not systematically found in both configurations. This is mainly linked to the processing strategy and the effect of measurement noise. However, for load condition T_4, a slight dissymmetry of the u_x and u_y fields can be observed. This indicates a stress state accompanied by crack initiation, probably from the vicinity of one of the free edges.

5.1.2 Out-of-plane displacement

The displacement field in the $\vec{z}$ direction is shown in Figure 19. While the first two stress states show a fairly linear evolution of displacement between interfaces and substrates, this is not the case for the last two states. A dissymmetry begins to appear in state T_3 and becomes more pronounced in T_4. This evolution is indeed synonymous with crack initiation, generating a very heterogeneous u_z displacement field and leading to failure

in the last stress state. This volumetric evolution provides invaluable information for understanding the degradation mechanisms of the adhesive joint.

	U_z (mm)
T_1	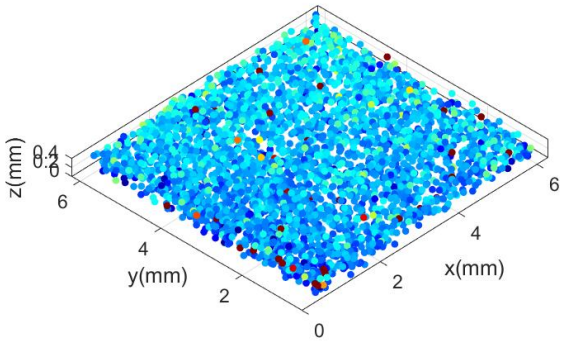
T_2	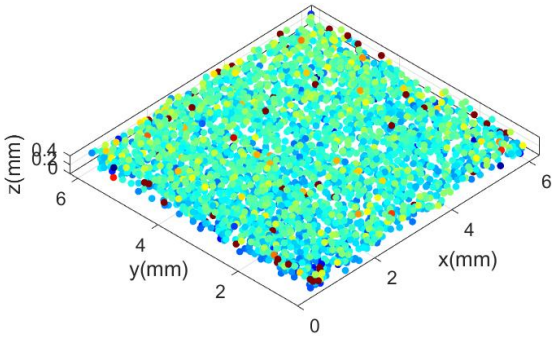
T_3	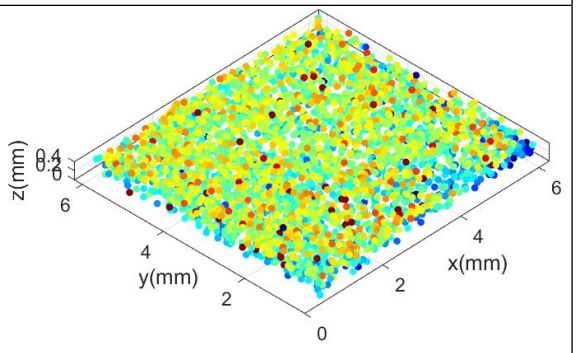
T_4	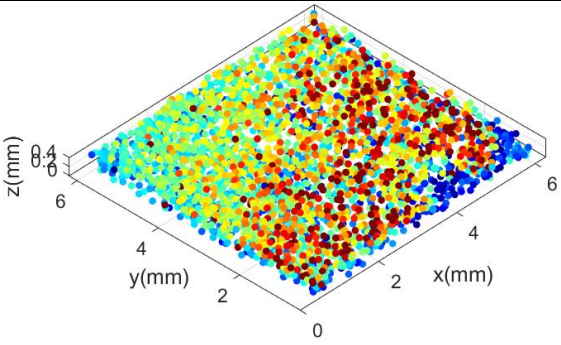

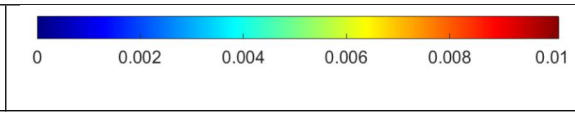

Figure 19 – Out-of-plane displacement field u_z [in mm]

5.2 Scarf 45°

The volumetric displacement field measurement strategy was also applied to an experimental tensile-shear configuration. The displacement field is expressed in the Cartesian coordinate system A $\vec{x}$ $\vec{y}$ $\vec{z}$ (Figure 1-b). In Figure 20, the displacement fields are plotted in the $\vec{x}$ and $\vec{y}$ for the two stress levels TS_1 and TS_2 (Figure 3-b). Displacements very close to zero are observed in the $\vec{x}$ direction, which is consistent with the kinematics of the test since in this direction there is virtually no displacement. This information is an important element in demonstrating the robustness of the method. On the other hand, a more heterogeneous displacement field was identified in the $\vec{y}$ direction, even for the first stress level (TS_1). These fields show once again that the stress state remains difficult to anticipate and sensitive to various parameters that can significantly influence maximum mechanical strength.

	U_x (mm)	U_Y (mm)
TS_1	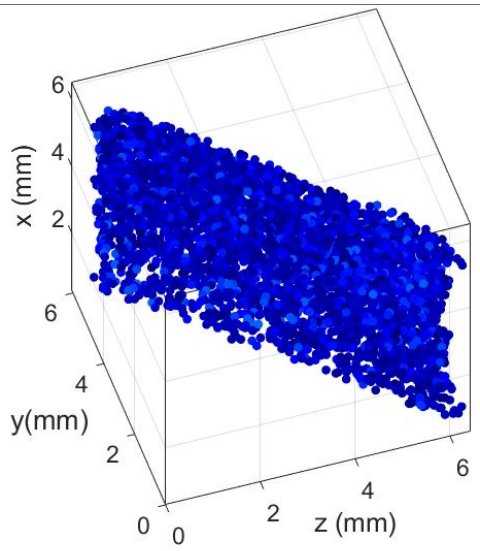	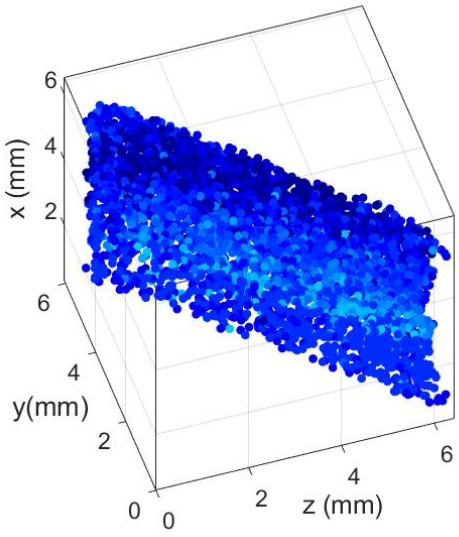
TS_2	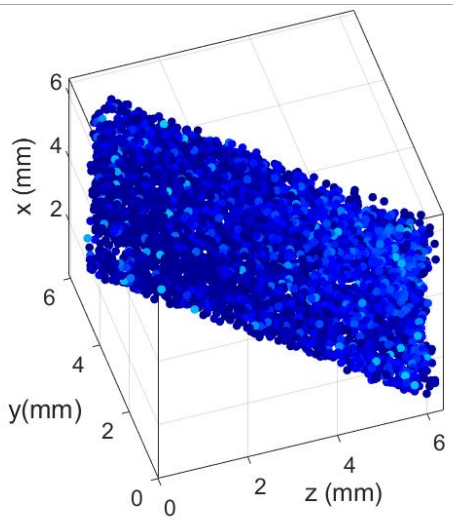	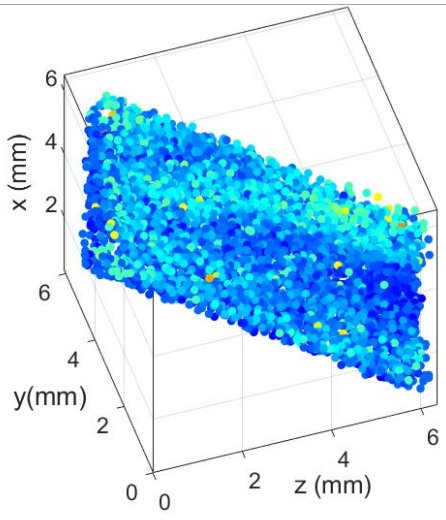
		

Figure 20 – Volumetric displacement fields [in mm] in the joint MS45 configuration, in the $\vec{x}$ and $\vec{y}$ directions

In concrete terms, in this configuration, fracture occurs relatively early, as the geometry of the sample used favors an extremely high edge effect. This edge effect is characterized by very high concentrations in the vicinity of the free edge. The presence of a pore in these stress concertation zones favors premature initiation and failure of the joint. This edge effect could be minimized if a geometry with beaks is implemented, as presented in [7]. The displacement field in the $\vec{z}$ direction is shown in Figure 21. Once again, one notices a field that is consistent with the kinematics of the load and relatively heterogeneous, exhibiting lateral variations similar to those observed for Uy. This means that the joint is subjected to a complex load condition, even for medium-intensity loads.

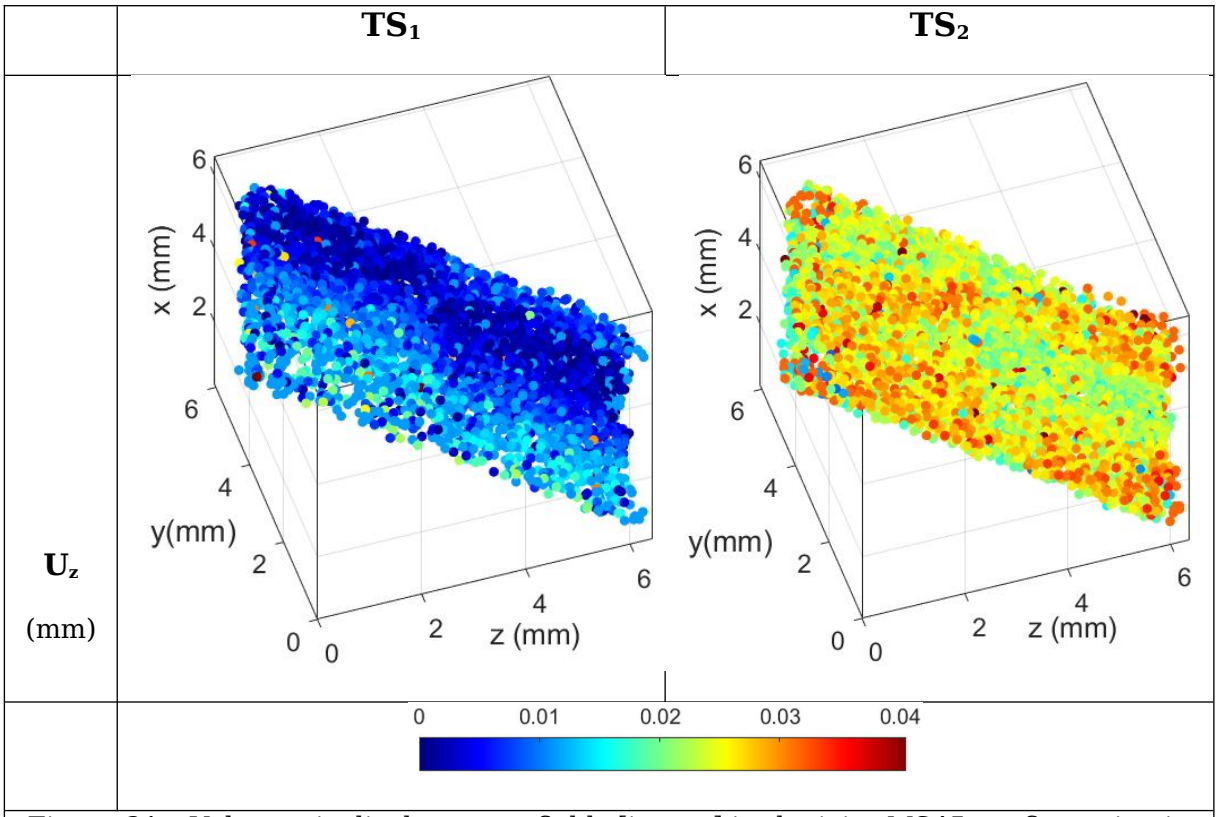

Figure 21 – Volumetric displacement fields [in mm] in the joint MS45 configuration in the $\vec{z}$ direction

6 Conclusion

In the article, the volume displacement field (within the Huntsman Araldite® 420 A/B structural epoxy adhesive joint) was measured based on micrometer-scale tomographic analyses. This adhesive joint highlights the presence of a population of rather spherical pore-type defects, characterized by an average equivalent diameter of around 50µm, and an average minimum distance between pores of around 95 µm.If we consider that these pores deform only slightly, thus behaving like rigid bodies, we can then consider that the displacement field thus determined is representative of the kinematics of the bonded sample studied. . In order to achieve a relatively high field density, we chose not to use digital volume correlation, which could obviously provide information, but to focus on developing a strategy based on particle tracking. Three methods have been proposed here, each with its advantages and disadvantages. These displacement measurement strategies were first validated on a synthetic volume configuration, enabling us to discriminate between the three proposed methods. It turns out that the Pore Correlation method is the best-performing strategy, giving conditions of difficulty similar to actual volumes. The robustness of this approach also opens up very interesting prospects for the future, enabling us to identify damage mechanisms at a local scale. The effects of pore voxelization, measurement noise, and sub-voxel displacement have been finely characterized, clearly showing the displacement resolutions achievable with these techniques. This strategy was applied to two real configurations: MS0 mini-scarf (tensile loading) and MS45 mini-scarf (proportional tensile and shear loading). These volumetric displacement fields, which are characterized by a point density of around 222 measurement points per mm^3, clearly show the various heterogeneities in the displacement field, enabling us to understand the highly complex state of stress within the adhesive. The effect of stress concentrations is mainly responsible for premature failure, clearly highlighted by the out-of-plane field of the joint associated with the MS0 configuration. The strategy proposed here opens up several very interesting outlooks. Firstly, the displacement field, with its consequent point density, can be used to determine deformation fields that are much more relevant to a more effective

understanding of the stress state. The strategy proposed here will be a valuable tool for investigating volume displacement fields in the context of hydric swelling, and subsequently identifying the swelling coefficient on a local scale using X-ray tomography. This coefficient of hydric swelling will enable us to estimate more precisely the hygrometric stresses that accompany the various adhesive structures immersed in seawater.

Acknowledgments

The authors are indebted to the Region Bretagne - SAD / France, for its financial support.

Declaration of competing interest

The authors declare that they have no known competing financial interests or personal relationships that could have appeared to influence the work reported in this paper.

References

[1] R. D. Adams. *Adhesive bonding: science, technology and applications*. Elsevier, 2005.

[2] L. F. M. da Silva. *Modeling of Adhesively Bonded Joints*. Springer-Verlag Berlin Heidelberg, 2008.

[3] D. A. Dillard. *Advances in structural adhesive bonding*. Elsevier, 2010.

[4] [17a] B. G. *Adhesion and Adhesives Technology*. Hanser Publications, 2012.

[5] J. Y. Cognard, R. Créac'hcadec, L. Sohier, and P. Davies. Analysis of the nonlinear behavior of adhesives in bonded assemblies-Comparison of TAST and Arcan tests. *International Journal of Adhesion & Adhesives*, 28:393–404, 2008. https://doi.org/10.1016/j.ijadhadh.2008.04.006

[6] J. Y. Cognard. Numerical analysis of edge effects in adhesively-bonded assemblies application to the determination of the adhesive behaviour. *Computers and Structures*, 86:1704–1717, 2008. https://doi.org/10.1016/j.compstruc.2008.02.003

[7] C. Badulescu, J. Cognard, R. Créac'hcadec, and P. Vedrine. Analysis of the low temperature dependent behaviour of a ductile adhesive under monotonic

tensile/compression–shear loads. *International Journal of Adhesion and Adhesives*, 36:56–64, 2012. https://doi.org/10.1016/j.ijadhadh.2012.03.009

[8] J.-Y. Buffiere, E. Maire, P. Cloetens, G. Lormand, R. Fouge, and A. Res. Characterization of internal´ damage in a MMC-p using X-ray synchrotron phase contrast microtomography. *Acta Materialia*, 47(5):1613–1625, 1999. https://doi.org/10.1016/S1359-6454(99)00024-5

[9] J. Y. Buffiere, E. Maire, J. Adrien, J.-P. Masse, and E. Boller. In situ experiments with x ray tomography: An attractive tool for experimental mechanics. *Experimental Mechanics*, 50:289–305, 2010. https://doi.org/10.1007/s11340-010-9333-7

[10] H. Toda, E. Maire, S. Yamauchi, H. Tsuruta, T. Hiramatsu, and M. Kobayashi. In situ observation of ductile fracture using X-ray tomography technique. *Acta Materialia*, 59(5):1995–2008, 2011. https://doi.org/10.1016/j.actamat.2010.11.065

[11] B. R. Pinzer, A. Medebach, H. J. Limbach, C. Dubois, M. Stampanoni, and M. Schneebeli. 3D characterization of three-phase systems using X-ray tomography: tracking the microstructural evolution in ice cream. *Soft Matter*, 8(17):4584, 2012. https://doi.org/10.1039/C2SM00034B

[12] B. Pollak. Experiences with planography**from the fort william sanatorium, *Diseases of the Chest*, 24(6):663 – 669, 1953.

[13] X. Liu and C. Bathias. Defects in squeeze-cast Al2O3/Al alloy composites and their effects on mechanical properties. *Composites Science and Technology*, 46(3):245–252, 1993. https://doi.org/10.1016/0266-3538(93)90158-D

[14] T. Breunig, S. Stock, A. Guvenilir, J. Elliott, P. Anderson, and G. Davis. Damage in aligned-fibre SiC/Al quantified using a laboratory X-ray tomographic microscope. *Composites*, 24(3):209–213, 1993.

[15] E. Maire, V. Carmona, J. Courbon, and W. Ludwig. Fast X-ray tomography and acoustic emission study of damage in metals during continuous tensile tests. *Acta Materialia*, 55(20):6806–6815, 2007. https://doi.org/10.1016/j.actamat.2007.08.043

[16] J. Adrien, E. Maire, N. Gimenez, and V. Sauvant-Moynot. Experimental study of the compression behaviour of syntactic foams by in situ X-ray tomography. *Acta Materialia*, 55(5):1667–1679, mar 2007. https://doi.org/10.1016/j.actamat.2006.10.027

[17] M. Pavan, T. Craeghs, R. Verhelst, O. Ducatteeuw, J. P. Kruth, and W. Dewulf. CT-based quality control of Laser Sintering of Polymers. *Case Studies in Nondestructive Testing and Evaluation*, 6:62–68, 2016. https://doi.org/10.1016/j.csndt.2016.04.004

[18] X. Wang, L. Zhao, J. Y. H. Fuh, and H. P. Lee. Effect of porosity on mechanical properties of 3D printed polymers: Experiments and micromechanical modeling based on X-ray computed tomography analysis. *Polymers*, 11(7), 2019. https://doi.org/10.3390/polym11071154

[19] V. Dumont, C. Badulescu, G. Stamoulis, J. Adrien, E. Maire A. Lefèvre and D. Thévenet. On the effect of the curing cycle on the creation of pores in structural adhesive joints by means of X-ray microtomography. *The Journal of Adhesion*, 97(12):1073–1106, 2021. https://doi.org/10.1080/00218464.2020.1728257

[20] V. Dumont, C. Badulescu, J. Adrien, N. Carrere, D. Thévenet, and E. Maire. Experimental investigation of porosities evolution in a bonded assembly by means of X-ray tomography. *Journal of Adhesion*, 97(6):528-552, 2019. https://doi.org/10.1080/00218464.2019.1685984

[21] V. Dumont, C. Badulescu, G. Stamoulis, J. Adrien, E. Maire, A. Lefèvre, and D. Thévenet, On the influence of mechanical loadings on the porosities of structural

epoxy adhesives joints by means of in-situ X-ray microtomography. *International Journal of Adhesion and Adhesives*, 99, 102568, 2020. https://doi.org/10.1016/j.ijadhadh.2020.102568

[22] M. Schwarzkopf and L. Muszynski. Strain distribution and load transfer in the polymer-wood particle bond in wood plastic composites. *Holzforschung*, 69(1):53–60, 2015. https://doi.org/10.1515/hf-2013-0243

[23] P. McKinley, D. Ching, F. Kamke, M. Zauner, and X. Xiao. Micro X-ray Computed Tomography of Adhesive Bonds in Wood. *Wood and Fiber Science*, 48(May):2–16, 2016.

[24] A. C. Kak and M. Slaney. *Principles of Computerized Tomographic Imaging*. Society of Industrial and Applied Mathematics, 2001.

[25] M. Sezgin. Survey over image thresholding techniques and quantitative performance evaluation. *Journal of Electronic Imaging*, 13(1):146–165, 2004. https://doi.org/10.1117/1.1631315

[26] S. Beucher and F. Meyer. *Mathematical Morphology in Image Processing*. Marcel dek edition, 1993.

[27] F. Meyer. Topographic distance and watershed lines. *Signal Processing*, 38:113–125, 1994.

[28] L. Grady. Random Walks for Image Segmentation. *IEEE Transactions on Pattern Analysis and*

Machine Intelligence, 28(11):1768–1783, 2006.

[29] N. Otsu. A Threshold Selection Method from Gray-Level Histograms. *IEEE Transactions on Systems, Man, and Cybernetics*, 9(1):62–66, 1979.

[30] N. C. Gallagher and G. L. Wise. A Theoretical Analysis of the Properties of Median Filters. *IEEE*

Transactions on Acoustics, Speech, and Signal Processing, 29(6):1136–1141, 1981.

[31] J. Schindelin, I. Arganda-Carreras, E. Frise, V. Kaynig, M. Longair, T. Pietzsch, S. Preibisch, C. Rueden, S. Saalfeld, B. Schmid, J.-Y. Tinevez, D. J. White, V. Hartenstein, K. Eliceiri, P. Tomancak, and A. Cardona. Fiji: an open-source platform for biological-image analysis. *Nat. Methods*, 9:676-682, 2012. https://doi.org/10.1038/nmeth.2019

[32] Leclerc, H., Périé, JN., Roux, S. et al. Voxel-Scale Digital Volume Correlation. Experimental Mechanics, Volume 51, 479–490 (2011). https://doi.org/10.1007/s11340-010-9407-6

[33] F. Gillard, R. Boardman, M. Mavrogordato, D. Hollis, I. Sinclair, F. Pierron, M. Browne, The application of digital volume correlation (DVC) to study the microstructural behaviour of trabecular bone during compression, Journal of the Mechanical Behavior of Biomedical Materials, Volume 29, 2014, Pages 480-499, https://doi.org/10.1016/j.jmbbm.2013.09.014.

[34] E. Ando, S. A. Hall, G. Viggiani, J. Desrues, and P. Bésuelle. Grain-scale experimental investigation of localised deformation in sand: A discrete particle tracking approach. *Acta Geotechnica*, 7(1):1–13, 2012. https://doi.org/10.1007/s11440-011-0151-6

[35] S. F. Nielsen, H. F. Poulsen, F. Beckmann, C. Thorning, and J. A. Wert. Measurements of plastic displacement gradient components in three dimensions

using marker particles and synchrotron X-ray absorption microtomography. *Acta Materialia*, 51(8):2407–2415, 2003. https://doi.org/10.1016/S1359-6454(03)00053-3

[36] Z. Zhou, C. E. Synolakis, R. M. Leahy, and S. M. Song. Calculation of 3D Internal Displacement Fields from 3D X-Ray Computer Tomographic Images. *Proceedings of the Royal Society A: Mathematical, Physical and Engineering Sciences*, 449(1937):537–554, 1995. https://doi.org/10.1098/rspa.1995.0057

[37] G. M. Bornhorst, K. Kostlan, R. Paul Singh, Particle Size Distribution of Brown and White Rice during Gastric Digestion Measured by Image Analysis, Journal of Food Science, Volume 78(9): 1383-1391, 2013, https://doi.org/10.1111/1750-3841.12228

[38] Wadell. Volume, shape, and roundness of quartz particles. *The Journal of Geology*, 43(3):250–280, 1935.

[39] T. Lavigne, A. Mazier, A. Perney, S.P.A. Bordas, F. Hild, J. Lengiewicz, Digital Volume Correlation for large deformations of soft tissues: Pipeline and proof of concept for the application to breast ex vivo deformations, Journal of the Mechanical Behavior of Biomedical Materials, 136, 105490, 2022, https://doi.org/10.1016/j.jmbbm.2022.105490.